Ceramics International 46 (2020) 28835–28843

Contents lists available at ScienceDirect

Ceramics International

journal homepage: www.elsevier.com/locate/ceramint

Synthesis and acetone sensing properties of copper (Cu^{2+}) substituted zinc ferrite hollow micro-nanospheres

Kaidi Wu[a], Yuling Lu[a], Yuhan Liu[a], Yan Liu[c], Ming Shen[b], Marc Debliquy[d], Chao Zhang[a,*]

[a] College of Mechanical Engineering, Yangzhou University, Yangzhou, 225127, China
[b] College of Chemistry and Chemical Engineering, Yangzhou University, Yangzhou, 225002, China
[c] Department of Endocrinology, Northern Jiangsu People's Hospital Affiliated to Yangzhou University, Yangzhou, 225001, China
[d] Materials Science Department, University of Mons, 56 Rue de l'Epargne, 7000, Mons, Belgium

ARTICLE INFO

Keywords:
$Cu_xZn_{1-x}Fe_2O_4$
Hollow micro-nanospheres
Gas sensor
Acetone

ABSTRACT

In this work, copper (Cu^{2+}) substituted zinc ferrite ($Cu_xZn_{1-x}Fe_2O_4$ ($0 \le x \le 1$)) hollow micro-nanospheres were synthesized using a facile solvothermal and annealing technology. We investigated the effects of Cu^{2+} substitution on morphology, structure and gas sensing properties of $Cu_xZn_{1-x}Fe_2O_4$ hollow micro-nanospheres. The results confirmed the successful substitution of Zn^{2+} with Cu^{2+} and the cations redistribution. In addition, the testing results revealed that $Cu_xZn_{1-x}Fe_2O_4$ ($0.25 \le x \le 1$) based sensors showed significantly enhanced responses to low concentration acetone vapor. Especially, $Cu_{0.75}Zn_{0.25}Fe_2O_4$ and $CuFe_2O_4$ displayed high responses of 2.37 and 2.43 to 0.8 ppm acetone at 125 °C respectively, while that of $ZnFe_2O_4$ was only 1.17. Moreover, $CuFe_2O_4$ demonstrated an excellent sensor response, ultra-low limit of detection and remarkable selectivity. The fast response speed and high stability of $CuFe_2O_4$ sensor further indicated that it was promising to apply for practical medical diagnosis. The enhanced sensing properties of $Cu_{0.75}Zn_{0.25}Fe_2O_4$ and $CuFe_2O_4$ sensors were explained by the effect of Cu^{2+} on lattice cation distribution, electron depletion layer thickness and adsorbing capacity.

1. Introduction

Acetone (C_3H_6O), the simplest structured saturated ketones, is extremely volatile, chemically active and flammable. It behaves toxic and threatens human health if its concentration exceeds 500 ppm [1]. Besides, acetone is the main ingredient of ketone body resulting from the fat metabolism process in human body [2]. Along with the continuous improvement of residents' living standards, the amount of diabetes patients increases worldwide. Based on the statistics reports from International Diabetes Federation (IDF), there were around 415 million people with diabetes worldwide in 2015. At present, for the diagnosis of diabetes, blood glucose is generally used to detect blood glucose concentration, which is an invasive and painful detection method. Moreover, these technologies also exist the problems of high cost, large size, and complicated operation, which are not suitable for developing portable diabetes detectors [3,4]. There exists acetone vapor in human exhaled breath, and the acetone content is positively related to the blood ketone content [5]. Therefore, the exhaled acetone concentration of diabetic patients (> 1.8 ppm) is higher than that of healthy people (0.39–0.9 ppm) [6]. In this view, respiratory analysis is a way to diagnose the disease by detecting the content of acetone in the human exhaled breath, which can realize the rapid and non-invasive diagnosis of diabetes [7,8].

Metal oxides semiconductor gas sensors, such as SnO_2 [9], ZnO [10], In_2O_3 [11], WO_3 [12] and Co_3O_4 [13], possess the characteristics of small size, low cost, simple operation, and high stability, which are the promising candidates for fabricating portable diabetes detector. Nevertheless, their low-concentration acetone sensing properties still need further improvement. Ternary zinc ferrite ($ZnFe_2O_4$) with a narrow bandgap (~1.94 eV) possesses remarkable physical properties and chemical stability, which have been applied in gas detection. For instance, $ZnFe_2O_4$ microspheres exhibited a fast response towards acetone vapor at around 200 °C [14]. Porous $ZnFe_2O_4$ nanorods prepared via simple hydrothermal method exhibited fine response towards acetone [15], mainly resulting from the pore structure and high specific surface area, but its practical detection limit was only about 1.5 ppm. Some researchers found that the doping of noble metal elements contributed to improving acetone properties through activation or

---

[*] Corresponding author. College of Mechanical Engineering, Yangzhou University, Huayang West Road 196, Yangzhou, 225127, Jiangsu Province, China.
E-mail address: zhangc@yzu.edu.cn (C. Zhang).
URL: http://zhangchao_cqu@hotmail.com (C. Zhang).

https://doi.org/10.1016/j.ceramint.2020.08.049
Received 29 May 2020; Received in revised form 24 July 2020; Accepted 5 August 2020

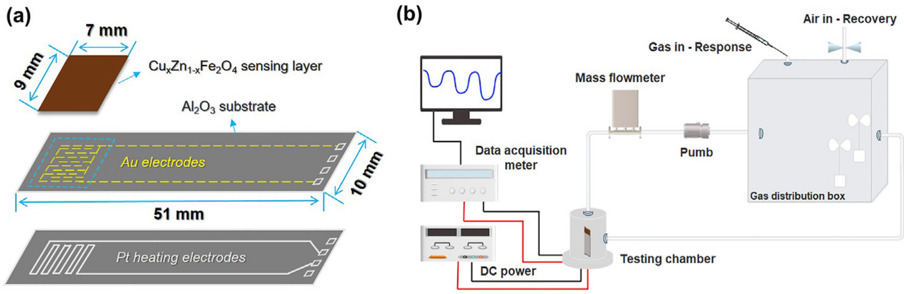

Fig. 1. (a) Schematic diagram of gas sensing element and (b) the whole gas sensing testing system.

cooperative effect. Zhang et al. fabricated Ag-$ZnFe_2O_4$ hollow spheres acetone sensor, exhibiting fine low-concentration acetone sensing performance at 175 °C [16]. Moreover, the doping or equivalent substitution of other metal elements, such as Co, Cd, Ni, and Cu, will also enable the corresponding gas sensors to detect gas accurately [17–19]. Mukherjee et al. investigated the sensing properties of $Cu_{0.5}Ni_{0.25}Zn_{0.25}Fe_2O_4$ and $Cu_{0.25}Ni_{0.5}Zn_{0.25}Fe_2O_4$ mixed metal ferrites. The results identified that the impact of more Cu^{2+} made a maximum sensitivity for acetone, and the impact of more Ni^{2+} made a better sensitivity for ethanol at room temperature [20]. In this view, combing the cooperation of metal elements with special micro-nanostructure may be an effective strengthen strategy for spinel ferrites gas sensors working under low temperatures.

As for the normal $ZnFe_2O_4$ crystal structure, Zn^{2+} and Fe^{3+} occupy in tetrahedral (A) and octahedral (B) interstitial spaces formed of oxygen ions. It is possible to generate lattice defects inside, which are in favor of gas sensing process. Furthermore, the spinel structure of transition metal cations inserting into anions sites shows good selectivity and fine response to reducing gases [21]. As well known, $CuFe_2O_4$ belongs to an inverse spinel with a narrow bandgap (~1.32 eV), which could be generally depicted as the formula: $[Fe^{3+}_{2-\alpha}]_A[Cu^{2+}Fe^{3+}_{\alpha}]_BO_4$ [22]. Inspired by the relative research, we prepared $ZnFe_2O_4$ hollow micro-nanospheres and realized the substitution of Cu^{2+} for Zn^{2+} and redistributed cations via a simple solvothermal process. The micromorphology, chemical composition of $Cu_xZn_{1-x}Fe_2O_4$ (x = 0, 0.25, 0.5, 0.75, 1) hollow micro-nanospheres and the effects of Cu^{2+} on phase structure and gas sensing properties were analyzed. $Cu_xZn_{1-x}Fe_2O_4$ (x = 0.25, 0.5, 0.75, 1) hollow micro-nanospheres showed significantly enhanced sensing properties to ppb level acetone at 125 °C. Moreover, the gas sensing mechanism and enhanced effect were also discussed.

2. Experimental

2.1. Synthesis of $Cu_xZn_{1-x}Fe_2O_4$ samples

$Cu_xZn_{1-x}Fe_2O_4$ ($0 \leq x \leq 1$) hollow micro-nanospheres were synthesized via a solvothermal and annealing process. 30 mL isopropanol and 8 mL glycerol were slowly added in a beaker and stirred for 1 h to obtain homogeneous solvent. Subsequently, 0.4042g $Fe(NO_3)_3 \cdot 9H_2O$ and the required amounts of $Cu(CH_3COO)_2 \cdot H_2O$, $Zn(CH_3COO)_2 \cdot 2H_2O$ were dissolved in the above solvent, then transferring it into Teflon-lined stainless-steel autoclave (100 mL) after magnetic stirring for 1 h, maintaining at 180 °C for 12 h. After naturally cooling down to 25 °C, the CuZn-Fe glycolate precursors were obtained through centrifuging and drying at 60 °C for 12 h. Ultimately, five samples were obtained after calcined at 400 °C for 2 h: $ZnFe_2O_4$ hollow micro-nanospheres (S1), $Cu_{0.25}Zn_{0.75}Fe_2O_4$ (S2), $Cu_{0.5}Zn_{0.5}Fe_2O_4$ (S3), $Cu_{0.75}Zn_{0.25}Fe_2O_4$ (S4) and $CuFe_2O_4$ (S5).

2.2. Material characterization

The phase structure of powders was identified through X-ray diffractometer (D8 Advance, Bruker) from 25° to 75° with the normal scan speed of $5^\circ \cdot min^{-1}$ and slow speed of $0.1^\circ \cdot min^{-1}$, respectively. The morphological and structural details were observed via Field-emission scanning electron microscopy (S4800II, Hitachi) and Transmission electron microscopy (JEM-2100). High-resolution TEM (HRTEM) information was obtained via field-emission transmission electron microscope equipped with energy dispersive X-ray spectrometry (Tecnai G2 F30 S-TWIN, FEI). The presence of oxygen vacancies is characterized by photoluminescence spectroscopy (PL, 325 nm He-Cd Lasers, ThermoFisher). The chemical bonding state was identified using Fourier transform infrared spectroscopy (Cary 640/670). The surface composition was determined via X-ray photoelectron spectroscope (Thermo Scientific ESCALAB 250Xi).

2.3. Fabrication of gas sensors and measurement

The corresponding powders (~ 2 mg) were firstly formed into slurry through mixing with deionized water, then it was coated on the upper side of Al_2O_3 ceramic substrate (C-MAC Micro Technology Company, Belgium), the detail of gas sensor element is schematically displayed in Fig. 1(a). $Cu_xZn_{1-x}Fe_2O_4$ (x = 0, 0.25, 0.5, 0.75 and 1) gas sensors were obtained after dried and aged at 150 °C for 24 h. The measurement system is displayed in Fig. 1(b). The required vapor concentration was calculated by the static evaporation of acetone liquid, as Formula (1):

$$V_x = \frac{V_0 \times c \times M}{22.4 \times \rho \times \varphi} \times 10^{-6} \tag{1}$$

V_x (μL) and V_0 (L) represents the volumes of the liquid and gas distribution box, respectively, c (ppm) is the corresponding vapor concentration, ρ (g/mL) is the liquid density, ϕ is the liquid purity, and M (g/mol) is the molecular weight of target gas.

The details of testing system can also be obtained in our reported works [6,23]. In addition, the response of gas sensor was the ratio of the resistance of sensors in air (R_a) to that in target gases (R_g). The response/recovery time is the time of 90% change in resistance.

3. Results and discussion

Fig. 2 displays the whole preparation process of $Cu_xZn_{1-x}Fe_2O_4$ (x = 0, 0.25, 0.5, 0.75 and 1) gas sensing element is schematically illustrated.

3.1. Structural and morphological characteristics

To verify the phase structure of synthesized $Cu_xZn_{1-x}Fe_2O_4$ samples, XRD patterns were investigated. In Fig. 3(a), the peaks of S1 and S5 were all matched well with cubic spinel $ZnFe_2O_4$ (JCPDS 22-1012) and inverse $CuFe_2O_4$ (JCPDS 34-0425). Moreover, $Cu_xZn_{1-x}Fe_2O_4$ (S2, S3 and S4) also retain standard spinel phases. Upon the increase of Cu,

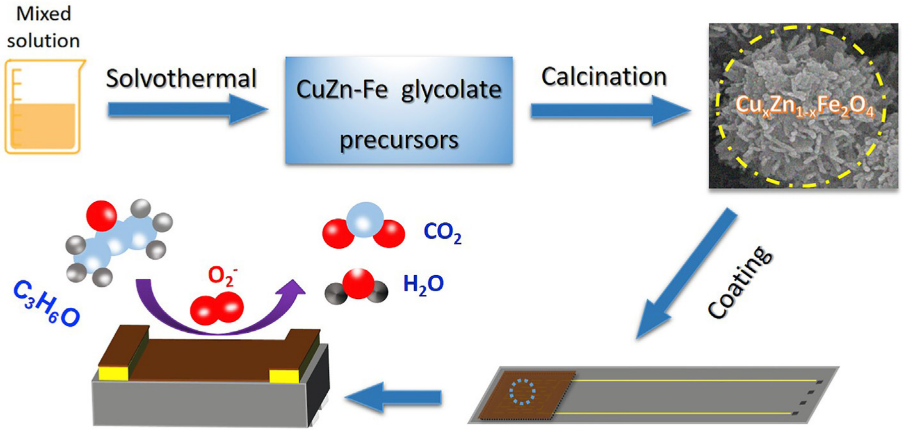

Fig. 2. Schematic diagram of the prepared process of $Cu_xZn_{1-x}Fe_2O_4$ hollow micro-nanospheres gas sensor.

several extra peaks with low intensity presented in the patterns, indicating that there exist a small number of secondary phases (Fe_2O_3 or CuO) in the $Cu_xZn_{1-x}Fe_2O_4$ samples. But all the main peaks were generally corresponding to the standard JCPDS cards patterns of $ZnFe_2O_4$ and $CuFe_2O_4$. In addition, to identify the substitution of Cu^{2+}, the amplified crystal face (311) of five samples was investigated and shown in Fig. 3(b). Owing to the ionic radius of Cu^{2+} (0.72 Å) is smaller than that of Zn^{2+} (0.74 Å), a lattice compression effect will happen and cause a decrease of lattice constant values [24]. Hence, these diffraction peaks shift to the low 2θ angle position, which is consistent with the reported work [24,25].

The surface morphology of $Cu_xZn_{1-x}Fe_2O_4$ was observed and FESEM images are displayed in Fig. 4. The incomplete spheres demonstrated the hollow structure of $Cu_xZn_{1-x}Fe_2O_4$. As illustrated in Fig. 4(a) and (e), pure $ZnFe_2O_4$ and $CuFe_2O_4$ both presented hollow micro-nanospheres (diameter: ~1 μm) structure, which mainly made up with nanoparticles (diameter: ~30 nm). Along with Cu substitution, the uniform diameters of spheres and hollow structure hardly changed, while the Cu-Zn mixed ferrites spheres were mainly composed of nanosheets instead of nanoparticles, as shown in Fig. 4(b–d) and the length and thickness of nanosheets were about 50 nm and 300 nm, respectively. This may result from the change in surface tension as the cations were redistributed [26]. Hence, the results indicate that the ratio of Cu to Zn makes an effect on adjusting morphological characteristics.

TEM results show further insight into structural and crystalline details of samples. Fig. 5(a–c) shows the TEM images of $Cu_xZn_{1-x}Fe_2O_4$ (x = 0, 0.75 and 1), it can be observed that the sphere surface was rough due to the assembled nanoparticles or nanosheets, and the sphere diameter was around 1 μm, which is corresponding to FESEM results. As for the absence of a hollow structure, it may result from the too-large shell thickness (~200 nm, Fig. 4(f)). Fig. 5(d) displays the lattice information of $CuFe_2O_4$. The lattice fringes spacing marked in Fig. 5(d) was 0.207 nm and 0.293 nm, representing (220) and (200) planes of $CuFe_2O_4$, respectively. And SAED results in Fig. 5(e) confirm the polycrystallinity, which is consistent with XRD conclusions. The STEM images and corresponding EDX element mappings of $CuFe_2O_4$ in Fig. 5(f) confirm the actual distribution of Cu, Fe and O in hollow micro-nanospheres.

FT-IR results of all samples are presented in Fig. 6(a). The vibrational frequency ($\upsilon1$) in the range of 600-500 cm^{-1} corresponds to M^{2+}-O^{2-} (M = Cu and Zn) and Fe^{3+}-O^{2-} stretching vibrations at the tetrahedral sites. The vibrational frequency ($\upsilon2$) ranging from 480 cm^{-1}–400 cm^{-1} are attributed to Fe^{3+}-O^{2-} and M^{2+}-O^{2-} (M = Cu and Fe) at octahedral sites [27,28]. The absorption bands that existed in around 1630 cm^{-1} indicate the bending mode of H_2O molecule and OH groups. Upon the increase of Cu contents, there exist weak absorption bands located at around 650 cm^{-1}, which are attributed to the multiplication and zone folding characteristic of CuO impurities [29]. The locations of vibrational bands shifted to the higher frequency side because of the increasing content of Cu with a smaller ionic radius. Overall, the results confirm the successful substitution Zn with Cu and the spinel structure of $Cu_xZn_{1-x}Fe_2O_4$.

The element chemical states of the $Cu_{0.75}Zn_{0.25}Fe_2O_4$ sample were determined via XPS to further identify the successfully obtained mixed ferrite. The electronic core levels of Cu 2p, Zn 2p, and Fe 2p in $Cu_{0.75}Zn_{0.25}Fe_2O_4$ were displayed by the high-resolution XPS spectra. Fig. 6(b) shows the Cu 2p results, in which the obvious peaks at about 932.09 eV and 952.01 eV were ascribed to Cu 2p3/2 and Cu 2p1/2, respectively [30]. The two core-level regions indicate the presence of Cu^{2+} on octahedral sites. The peaks at around 933.21 eV and 952.21eV represent that small amounts of Cu^{2+} occupied on tetrahedron sites [31]. Moreover, the satellite peaks of Cu 2p identify copper that exists

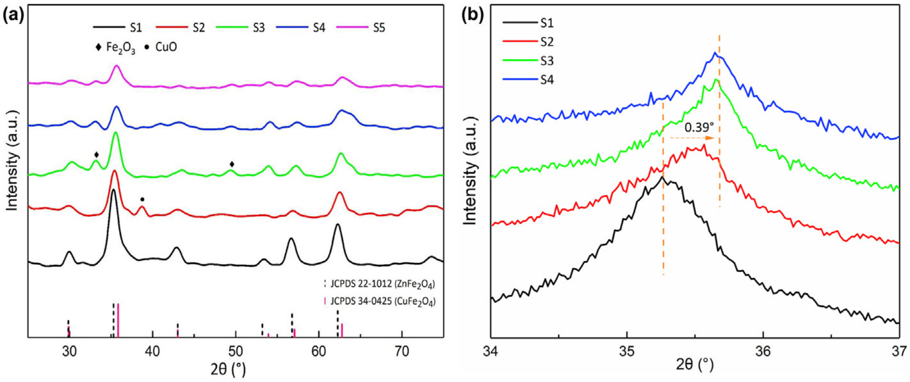

Fig. 3. XRD patterns of (a) normal scan results of five samples and (b) slow-speed scan analysis of S1, S2, S3 and S4 from 34° to 37°.

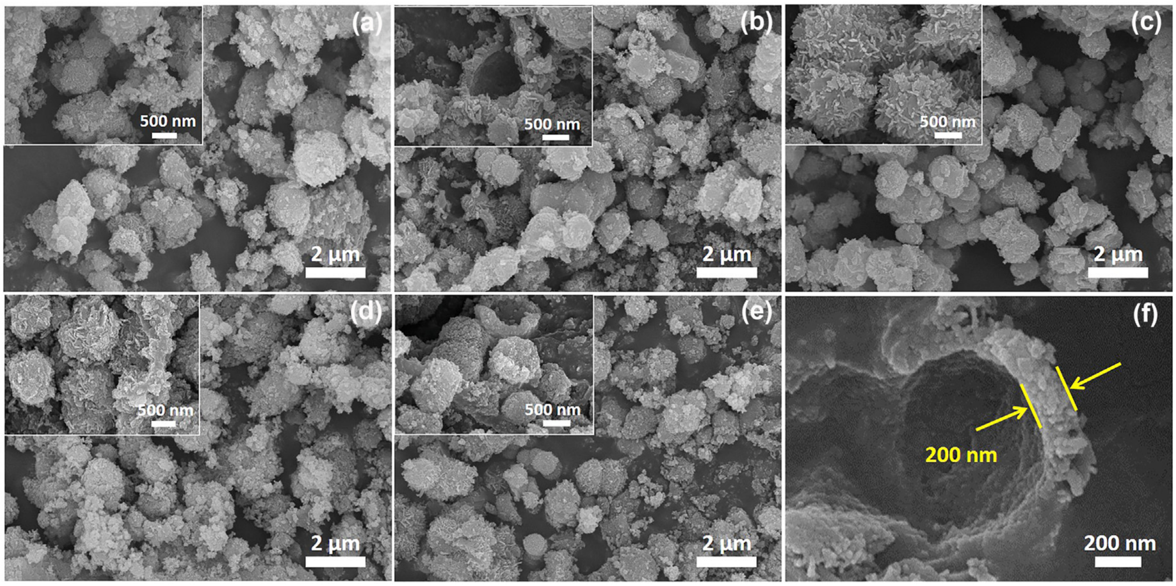

Fig. 4. FESEM images of $Cu_xZn_{1-x}Fe_2O_4$: (a) S1 (b) S2 (c) S3 (d) S4 and (e) S5, (f) high-resolution analysis of broken S5.

in +2 valence. Fig. 6(c) displays two fitted peaks of 1021.82 eV and 1044.22 eV, representing Zn 2p3/2 and Zn 2p1/2 of $Cu_{0.75}Zn_{0.25}Fe_2O_4$, respectively. It demonstrates Zn also exists in tetrahedron sites with the oxidation state of +2 valence [32]. In addition, the atomic ratios of Cu and Zn are 1.29% and 0.36%, respectively. Therefore, the contents ratio of Cu to Zn is about 3.58:1, which approaches to the theoretical ratio of 3:1. In Fig. 6(d), due to Fe 2p1/2 possesses lower angular momentum value than Fe 2p3/2, the former is located at a higher binding energy region in XPS spectra of $Cu_{0.75}Zn_{0.25}Fe_2O_4$. The two fitted by two Gaussian peaks at around 710 eV and 723 eV are assigned to the spin-orbit doublets of Fe 2p3/2 and Fe 2p1/2, demonstrating the existence of Fe^{3+}. The two satellite peaks of Fe 2p further identify that the iron element exists in +3 valence [33]. In addition, the peaks located at 710.25 eV could be associated with Fe^{3+} in octahedral sites, while the peaks located at 713.48 eV indicated that Fe^{3+} existed in tetrahedral sites [34]. The spin-orbit doublets are normally associated with asymmetric satellite peaks, suggesting a possible presence of corresponding ion states. Therefore, the satellite peak centered at binding energies of 715.95 eV without corresponding Fe^{2+} 2p3/2 peaks of FeO and Fe_3O_4 suggests that there generating Fe^{2+} by electron hopping between Fe^{3+} and Fe^{2+} in the spinel structure lattice [35]. In other words, the cations distribution of the mixed ferrite was adjusted via the substitution of

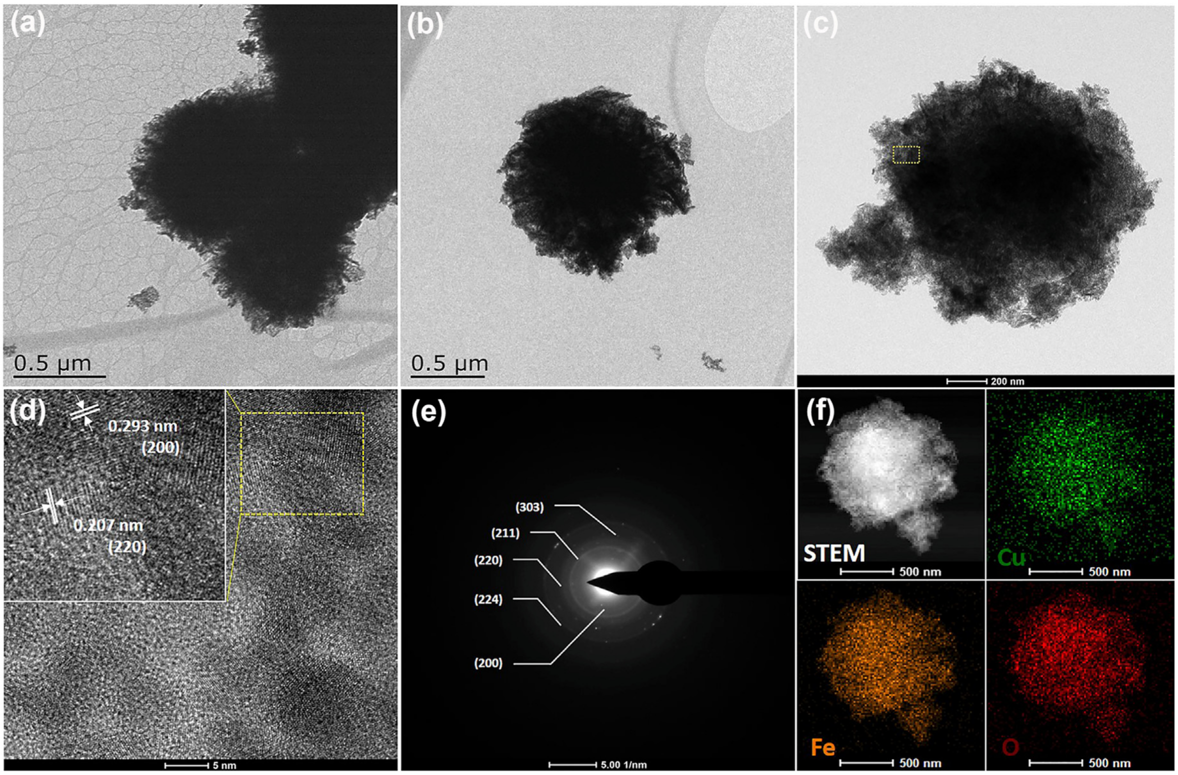

Fig. 5. TEM images of (a) S1 and (b) S2, (c–e) HR-TEM images of S5, (f) STEM-EDX images of S5.

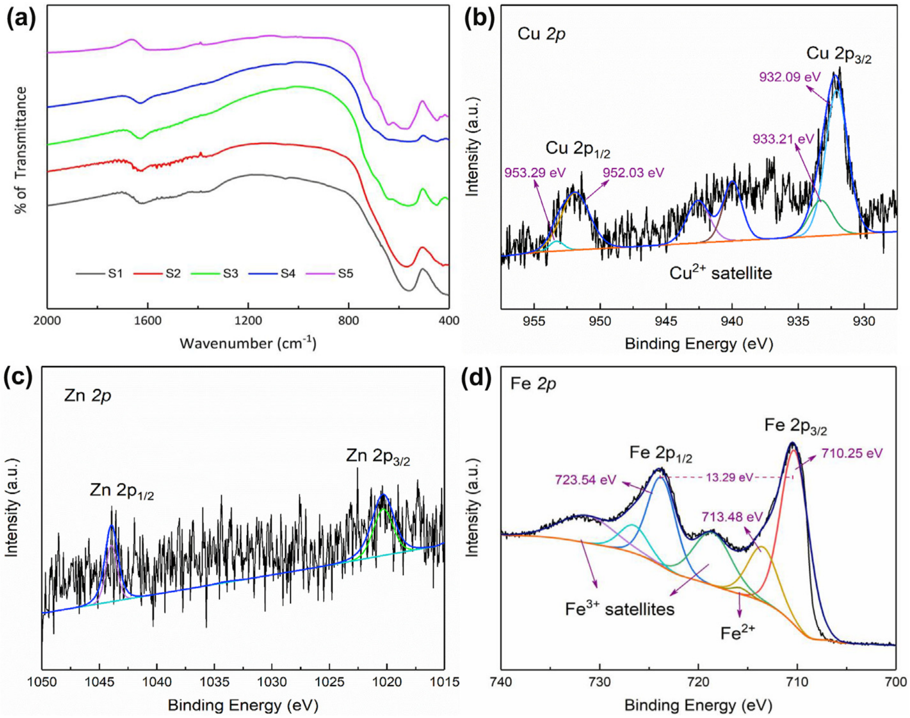

Fig. 6. (a) FTIR spectra of $Cu_xZn_{1-x}Fe_2O_4$ samples; Elements chemical states of the $Cu_{0.75}Zn_{0.25}Fe_2O_4$ sample determined via XPS: (b) Cu 2p, (c) Zn 2p and (d) Fe 2p.

Zn^{2+} with Cu^{2+}.

3.2. Gas sensing characteristics

The sensor response of $Cu_xZn_{1-x}Fe_2O_4$ to 1 ppm acetone was tested under different temperatures ranging from 100 °C to 225 °C. Fig. 7(a) shows that the operating temperature significantly affected all gas sensors, resulting from the heating effect on surface activation energy of the sensing layer and gas-solid phase reaction [36]. Once the temperature increased further to be higher than the optimum temperature, it will cause fast gas desorption. Hence, all response curves as a function of temperature show a “rise - peak value - reduce” tendency. The results demonstrated the introduction of Cu lowered optimum operating temperature from 150 °C to 125 °C, and $CuFe_2O_4$ (S5) exhibited the highest value (2.53) at 125 °C, indicating the substitution of Cu^{2+} played a vital role in improving sensing properties of $Cu_xZn_{1-x}Fe_2O_4$ hollow micro-nanospheres sensors.

Aiming to study the dynamic acetone sensing performance, S1, S4, and S5 gas sensors were fabricated and tested at 125 °C. Fig. 7(b) showed that all the sensors exhibit reversible resistance change along with the recycling process of air in and acetone in. The detailed relationship between response values and acetone concentrations is plotted in Fig. 7(c). The response of S4 and S5 sensors both show clearly higher values than that of S1 sensor. As for the best $CuFe_2O_4$ acetone sensor, the response towards 10 ppm acetone (9.92) is around 5.9 times higher than that of $ZnFe_2O_4$ (1.68). Additionally, it is interesting that S4 and S5 both exhibit ideal responses to 0.8 ppm acetone, which are 2.37 and 2.43, respectively. However, upon the increasing acetone concentration, the response of S4 is much lower than that of S5 gas sensor. Hence, we chose $CuFe_2O_4$ (S5) gas sensor to investigate further corresponding sensing properties.

Linearity is an important property factor of high-performance gas sensors, which is also one of the criteria for evaluating whether rapid quantitative analysis can be achieved. Fig. 8(a) depicts the dual logarithmic linear fitting data of pristine $ZnFe_2O_4$ and $CuFe_2O_4$ versus various concentrations of acetone. The linear coefficients of correlation between two gas sensors are $R_1^2 = 0.8823$ and $R_5^2 = 0.9499$, respectively. We can find that the full substitution of Cu^{2+} contributes to obtaining better sensor linearity. According to medical diagnostic literature, the acetone concentration in normal human exhaled breath ranges from 0.39 to 0.9 ppm. Hence, as another important parameter representing the sensing properties, limitation of detection (LOD) of both gas sensors were assessed. Owing to the limitation of the gas sensing testing system, we got the LOD values through theoretical

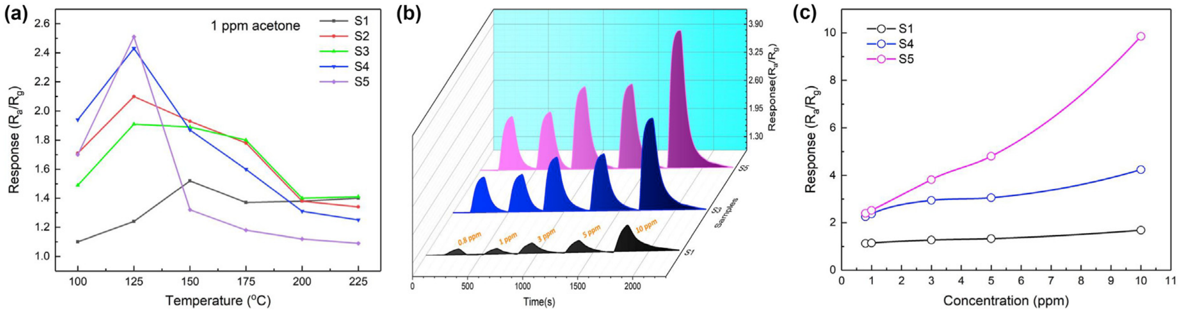

Fig. 7. (a) Sensor responses of $Cu_xZn_{1-x}Fe_2O_4$ to 1 ppm acetone at 100–225 °C; (b) Dynamic sensing performance of S1, S4 and S5 gas sensors to 0.8–10 ppm acetone at 125 °C, (c) response values versus acetone concentration.

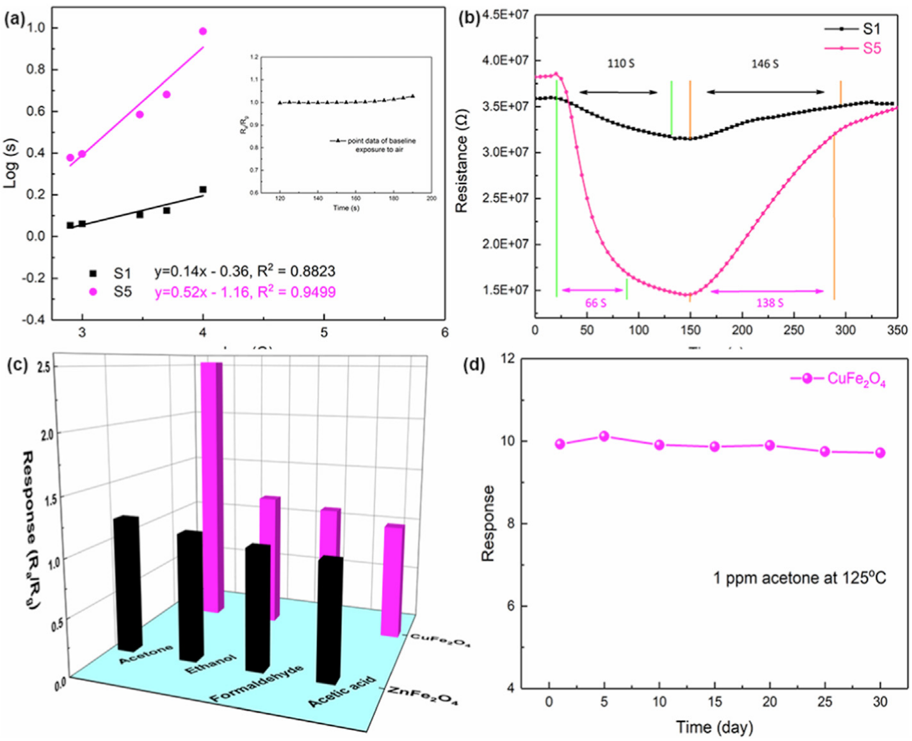

Fig. 8. (a) Dual logarithmic linear fitting data of $ZnFe_2O_4$ and $CuFe_2O_4$ versus 0.8–10 ppm acetone, (b) response/recovery time curves of both sensors to 1 ppm acetone at 125 °C, (c) Selectivity of $ZnFe_2O_4$ and $CuFe_2O_4$ to 1 ppm target gases at 125 °C, (d) Response of $CuFe_2O_4$ to 1 ppm acetone at 125 °C gas sensor in 30 days.

calculation. The gas response of resistance-type metal oxide semiconductors sensor can be depicted as the following:

$$S = A_{tg}\,(P_{tg})^{\beta} \tag{2}$$

where S is the response defined as R_a/R_g, A_{tg} is the prefactor, P_{tg} denotes the partial pressure of target gas, β represents the exponent [37]. As a result, through the logarithm process for Formula (2), there exists a linear relation between logarithm response values (log S) with logarithm acetone concentration (log C, ppb), which can be expressed as Formula (3) [38], A'_g is the intercept value, and β will become the slope. The practical linear relationship had been shown in Fig. 8(a).

$$\mathrm{Log}\ S = A'_g + \beta \mathrm{Log}\ (C) \tag{3}$$

$$LOD_{ppb} = 3\ RMS_{noise}/k \tag{4}$$

According to the IUPAC definition, the theoretical LOD could be calculated via Formula (4) [39], in which RMS_{noise} (0.0089) is the gas sensor noise calculated via root-mean-square deviation processing on the 15 baseline data taken exposure to air in Fig. 8(a), k is the slopes of corresponding linear fitting curves, which are 0.14 and 0.52 for $ZnFe_2O_4$ and $CuFe_2O_4$. So that, the LOD value of $ZnFe_2O_4$ and $CuFe_2O_4$ sensors is extrapolated to be around 0.19 ppb and 0.051 ppb, respectively, indicating that the substitution of Cu^{2+} help obtaining higher sensitivity and lower limitation of detection.

Fig. 8(b) exhibits the response/recovery curves of S1 and S5 sensors towards acetone of 1 ppm under 125 °C. The response/recovery time of $CuFe_2O_4$ sensors is 66 s and 136 s, which are smaller than that of $ZnFe_2O_4$ sensors (110 s and 146 s). It also proves that the enhanced effect of Cu^{2+} on sensing properties. As summarized in Table 1, compared with previously reported spinel ferrites based gas sensors, $Cu_{0.75}Zn_{0.25}Fe_2O_4$ and $CuFe_2O_4$ hollow micro-nanospheres showed excellent low-concentration acetone sensing properties at a lower temperature.

High selectivity and stability are the challenges of the practical gas sensor, especially for detecting the ultra-low concentration target gas. Therefore, acetone, ethanol, formaldehyde, and acetic acid, four target gases of 1 ppm were tested at 125 °C. Fig. 8(c) demonstrates clearly that the acetone selectivity of $CuFe_2O_4$ sensor becomes significantly better than $ZnFe_2O_4$ sensor. It may result from the lowest bond dissociation energy of target gases (acetone, 52 kJ/mol; ethanol, 462 kJ/mol; formaldehyde, 368 kJ/mol and acetic acid, 685 kJ/mol) and improved adsorption capacity of $CuFe_2O_4$, in other words, the reaction between chemisorbed oxygen anions and acetone molecules is easier and preferable [45,46].

Furthermore, $CuFe_2O_4$ sensor was exposed to 10 ppm acetone for a month to check the performance stability. Fig. 8(d) depicts that the sensor response values maintain at around 9.9, displaying excellent long term stability of $CuFe_2O_4$ gas sensor.

3.3. Acetone sensing mechanism

The gas sensing mechanism can be illustrated by the commonly accepted n-type semiconductor resistance change resulting from the adsorption/desorption and reaction of surface gas molecules [47]. Once exposure to air under 125 °C, oxygen molecules subsequently adsorb on the surface and transform to oxygen ions ($O^-_{2(ads)}$) through capturing free electrons from conduction band of $Cu_xZn_{1\text{-}x}Fe_2O_4$ hollow micro-nanospheres (Formula (6)). Subsequently, there will generate an electron depletion layer and lead to increased resistance. After injecting acetone liquid, the oxygen species will react with acetone molecules to generate carbon dioxide and water molecules (Formula (7)). Meanwhile, electrons will be released back and resistance will decrease at the time. When the resistance level becomes stable, air will be introduced again to recover.

$$O_2\ (gas) \rightarrow O_2\ (ads) \tag{5}$$

$$e^-\ (Cu_xZn_{1\text{-}x}Fe_2O_4) + O_2\ (ads) \rightarrow O_2^-\ (ads) \tag{6}$$

$$CH_3COCH_3 + 4O_2^-\ (ads) \rightarrow 3CO_2 + 3H_2O + 4e^- \tag{7}$$

The improved gas sensing performance of $Cu_xZn_{1\text{-}x}Fe_2O_4$ (x = 0.25, 0.5, 0.75 and 1) than $ZnFe_2O_4$ can be ascribed to the effect of Cu^{2+} on

Table 1
Comparisons of various metal oxides based acetone sensor.

Materials	Micromorphology	Temperature (°C)	Concentration (ppm)	Definition of response	Response	Ref.
$ZnFe_2O_4$	macroporous spheres	275 °C	3.22	R_a/R_g	1.20	[40]
$NiFe_2O_4$	nanocubes	160 °C	1	R_g/R_a	1.90	[41]
$CuFe_2O_4$	nanspheres	250 °C	1	R_a/R_g	1.90	[22]
$CoFe_2O_4$	nanoparticles	225 °C	5	R_a/R_g	3.20	[42]
0.25 wt% Ag-$ZnFe_2O_4$	hollow spheres	175 °C	0.8	R_a/R_g	1.40	[16]
0.5% Pt-$CuFe_2O_4$	nanotubes	300 °C	5	R_a/R_g	3.80	[43]
$Cu_{0.5}Ni_{0.25}Zn_{0.25}Fe_2O_4$	nanocrystalline	25 °C	500	R_a/R_g	1.77	[20]
4 wt% Ce-$CoFe_2O_4$	nanocrystalline	225 °C	100	R_g/R_a*100%	177%	[44]
$Cu_{0.75}Zn_{0.25}Fe_2O_4$	Hollow micro-nanospheres	125 °C	0.8	R_a/R_g	2.37	This work
$CuFe_2O_4$		125 °C	0.8	R_a/R_g	2.43	This work

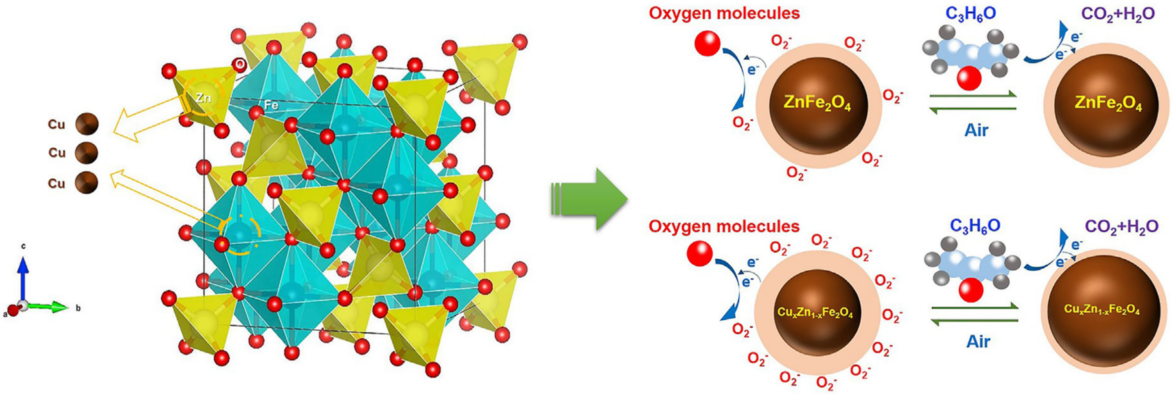

Fig. 9. Gas sensing enhanced mechanism of the $Cu_xZn_{1-x}Fe_2O_4$ hollow micro-nanospheres gas sensor.

the electron depletion layer thickness, as shown in Fig. 9. According to the XPS results of Cu 2p, the substituted Cu^{2+} insert the tetrahedron and octahedral sites of $ZnFe_2O_4$ crystal structure. Due to the forbidden bandwidths of $CuFe_2O_4$ and $ZnFe_2O_4$ are ~1.32 eV and ~1.94 eV, respectively, it may narrower the forbidden bandwidth of mixed ferrites, resulting in an improvement of electrons freedom [48]. Hence, it will be more easily for adsorbed oxygen to capture the electrons in the conduction bands of $Cu_xZn_{1-x}Fe_2O_4$, which causes an increase of the electron depletion layer thickness and O_2^- content on the surface of $Cu_xZn_{1-x}Fe_2O_4$. Simultaneously, Formula (7) will more efficiently occur and the sensing properties will also be improved.

In addition, the substitution of Cu^{2+} also adjusts the cations distribution of spinel $Cu_xZn_{1-x}Fe_2O_4$ lattice. As analyzed in XPS section, the electron hopping between Fe^{3+} and Fe^{2+} ions belongs to a kind of n-type conduction: $Fe^{3+} \leftrightarrow Fe^{2+} + e^-$. This may cause enhancement of the surface activity to oxygen molecules [49]. Furthermore, the copper incorporated in spinel crystal lattice could act as an electroactive dopant to improve the electronic characteristic [50]. Hence, the presence of Cu^{2+} and Fe^{2+} contributes to increasing oxygen adsorption capacity of ferrites which in turn results in a better sensing property.

The oxygen species and vacancies in samples are investigated to explain the improved sensing properties through PL and XPS. In Fig. 10(a), two peaks observed in the visible region in emission spectra of all the samples correspond to the presence of defects and oxygen vacancies. The first peak observed at 612 nm may correspond to direct band edge transition. Due to the limited instrument detection range, the absolute second peak cannot be observed, it should be observed at a lower wavelength, which confirms the presence of defects states (such as oxygen vacancies, interstitials, etc.) in the forbidden energy gap [51]. The presence of large oxygen vacancies can offer more electrons for the chemical adsorption of oxygen, increasing the efficiency of electrons transfer and sensitivity [40]. As shown in Fig. 10(b), the O1s spectra of S4 are fitted with three regions centered at 529.63 eV (O_L), 531.21 eV (O_V) and 532.25 eV (O_C). O_L peak is mainly assigned to lattice oxygen of S4 [40]. O_V peak is related to the oxygen defect in the spinel crystal. O_C peak is ascribed to the surface chemisorbed oxygen ions [52]. In Fig. 10(c), the O1s spectra of S5 are also fitted with three peaks located at similar binding energies: 529.63 eV (O_L), 531.13 eV (O_V) and 532.41 eV (O_C). We can find that $CuFe_2O_4$ sample obtained larger amounts of chemisorbed oxygen, resulting in a further reduction of electron concentration, which is also favorable for the gas-solid phase reaction. Furthermore, the unique hollow structure also contributes to providing enough active sites. Thus, the sensor response of $CuFe_2O_4$ is higher than that of $Cu_{0.75}Zn_{0.25}Fe_2O_4$.

4. Conclusion

$Cu_xZn_{1-x}Fe_2O_4$ ($0 \le x \le 1$) hollow micro-nanospheres were synthesized using a facile solvothermal and annealing technology. The results confirmed the successful substitution of Zn^{2+} with Cu^{2+} and the cation redistribution. The mixed ferrites sensors showed higher responses to 1 ppm acetone at 125 °C than pristine $ZnFe_2O_4$. Moreover, $Cu_{0.75}Zn_{0.25}Fe_2O_4$ and $CuFe_2O_4$ displayed high responses of 2.37 and 2.43 to 0.8 ppm acetone at a low temperature (125 °C), while that of $ZnFe_2O_4$ was only 1.17. Apart from the excellent sensing performance towards acetone ranging from 0.8 to 10 ppm, $CuFe_2O_4$ sensor also demonstrated an ultra-low limit of detection, remarkable selectivity and stability. The enhanced sensing properties of $Cu_{0.75}Zn_{0.25}Fe_2O_4$ and $CuFe_2O_4$ sensors were illustrated by the effect of Cu^{2+} on lattice cation distribution, electron depletion layer thickness and adsorbing capacity. Hence, $CuFe_2O_4$ hollow micro-nanospheres gas sensor is promising to apply for practical medical diagnosis.

Declaration of competing interest

The authors declare that they have no known competing financial interests or personal relationships that could have appeared to influence the work reported in this paper.

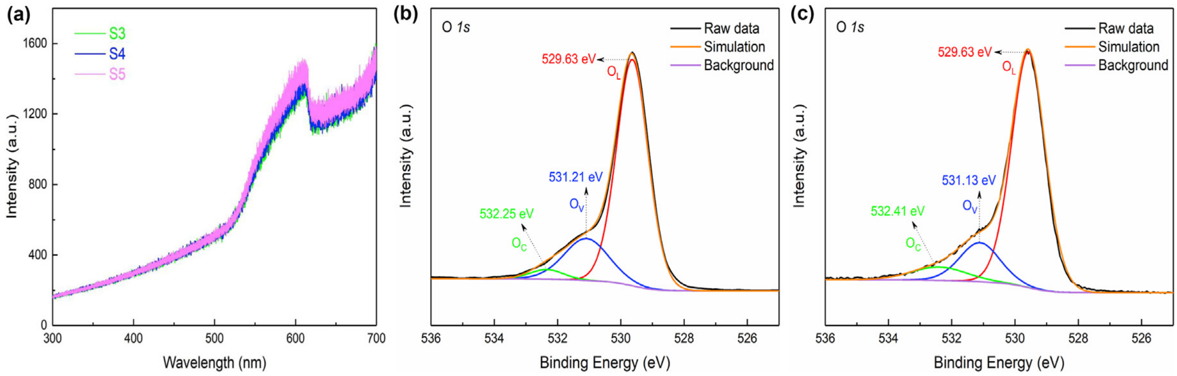

Fig. 10. (a) PL spectra of $Cu_xZn_{1-x}Fe_2O_4$ ($0.5 \le x \le 1$); O1s spectra of (b) $Cu_{0.75}Zn_{0.25}Fe_2O_4$ (S4) and (c) $CuFe_2O_4$ (S5).

Acknowledgment

This work is supported by the National Key Research and Development Program of China under Grant No. 2017YFE0115900, the Natural Science Foundation of China under Grant No. 51872254 and the Yangzhou City-Yangzhou University Cooperation Foundation under Grant No. YZU201801.

References

[1] D.Z. Zhang, Y.B. Jin, H.N. Chen, Y.W. Luo, Y. Zhang, Carbon microsphere-templated synthesis of $ZnCo_2O_4$ hollow spheres functionalized with Ag nanoparticles for sub-ppm-level acetone gas detection, Ceram. Int. 46 (2020) 15176–15182, https://doi.org/10.1016/j.ceramint.2020.03.054.

[2] R. Yoo, Y. Park, H. Jung, H.J. Rim, S. Cho, H.S. Lee, W. Lee, Acetone-sensing properties of doped ZnO nanoparticles for breath-analyzer applications, J. Alloy, Compd 803 (2019) 135–144, https://doi.org/10.1016/j.jallcom.2019.06.254.

[3] W. Miekisch, J.K. Schubert, From highly sophisticated analytical techniques to life-saving diagnostics: technical developments in breath analysis, Trac. Trends Anal. Chem. 25 (2006) 665–673, https://doi.org/10.1016/j.trac.2006.05.006.

[4] C. Turner, Techniques and issues in breath and clinical sample headspace analysis for disease diagnosis, Bioanalysis 8 (2016) 677–690, https://doi.org/10.4155/bio.16.22.

[5] V. Saasa, T. Malwela, M. Beukes, M. Mokgotho, C.P. Liu, B. Mwakikunga, Sensing technologies for detection of acetone in human breath for diabetes diagnosis and monitoring, Diagnostics 8 (2018) 12, https://doi.org/10.3390/diagnostics8010012.

[6] K.D. Wu, Y.F. Luo, Y. Li, C. Zhang, Synthesis and acetone sensing properties of $ZnFe_2O_4$/rGO gas sensors, Beilstein J. Nanotechnol. 10 (2019) 2516–2526, https://doi.org/10.3762/bjnano.10.242.

[7] M. Righettoni, A. Tricoli, S.E. Pratsinis, Si, WO_3 sensors for highly selective detection of acetone for easy diagnosis of diabetes by breath analysis, Anal. Chem. 82 (2010) 3581–3587, https://doi.org/10.1021/ac902695n.

[8] T.S. Wang, S.F. Zhang, Q. Yu, S.P. Wang, P. Sun, H.Y. Lu, F.M. Liu, X. Yan, G.Y. Lu, Novel self-assembly route assisted ultra-fast trace volatile organic compounds gas sensing based on three-dimensional opal microspheres composites for diabetes diagnosis, Acs Appl. Mater. Inter. 10 (2018) 32913–32921, https://doi.org/10.1021/acsami.8b13010.

[9] G.J. Li, Z.X. Cheng, Q. Xiang, L.M. Yan, X.H. Wang, J.Q. Xu, Bimetal PdAu decorated SnO_2 nanosheets based gas sensor with temperature-dependent dual selectivity for detecting formaldehyde and acetone, Sens. Actuators, B 283 (2019) 590–601, https://doi.org/10.1016/j.snb.2018.09.117.

[10] J. Zhou, F.L. Gong, H.X. Wang, Y.H. Xiao, F. Li, W.N. Mai, 3D mace-like hierarchical ZnO nanoarchitecture constructed with microrod bundles and porous single-crystalline nanosheets for acetone sensors with enhanced performances, Mater. Sci. Eng. B-Adv. 225 (2017) 68–74, https://doi.org/10.1016/j.mseb.2017.08.009.

[11] Y.L. Wang, P.F. Cheng, X. Li, C. Wang, C.H. Feng, G.Y. Lu, Revealing the relationship between the Au decoration method and the enhanced acetone sensing performance of a mesoporous In_2O_3-based gas sensor, J. Mater. Chem. C 8 (2020) 78–88, https://doi.org/10.1039/c9tc05082e.

[12] W.S. Zhang, Y. Fan, T.W. Yuan, B. Lu, Y.M. Liu, Z.X. Li, G.J. Li, Z.X. Cheng, J.Q. Xu, Ultrafine tungsten oxide nanowires: synthesis and highly selective acetone sensing and mechanism analysis, Acs Appl. Mater. Inter. 12 (3) (2020) 3755–3763, https://doi.org/10.1021/acsami.9b19706.

[13] T.T. Zhou, T. Zhang, J.A. Deng, R. Zhang, Z. Lou, L.L. Wang, P-type Co_3O_4 nanomaterials-based gas sensor: preparation and acetone sensing performance, Sens. Actuators, B 242 (2017) 369–377, https://doi.org/10.1016/j.snb.2016.11.067.

[14] F.D. Qu, W.N. Shang, T. Thomas, S.P. Ruan, M.H. Yang, Self-template derived $ZnFe_2O_4$ double-shell microspheres for chemresistive gas sensing, Sens. Actuators, B 265 (2018) 625–631, https://doi.org/10.1016/j.snb.2018.03.108.

[15] L. Li, J.F. Tan, M.H. Dun, X.T. Huang, Porous $ZnFe_2O_4$ nanorods with net-worked nanostructure for highly sensor response and fast response acetone gas sensor, Sens. Actuators, B 248 (2017) 85–91, https://doi.org/10.1016/j.snb.2017.03.119.

[16] C. Zhang, Q.D. Wu, B.B. Zheng, J.J. You, Y.F. Luo, Synthesis and acetone gas sensing properties of Ag activated hollow sphere structured $ZnFe_2O_4$, Ceram. Int. 44 (2018) 20700–20707, https://doi.org/10.1016/j.ceramint.2018.08.064.

[17] H.R. Ebrahimi, H. Usefi, H. Emami, G.R. Amiri, Synthesis, characterization, and sensing performance investigation of copper cadmium ferrite nanoparticles, Ieee T. Magn. 54 (10) (2018) 4000905, , https://doi.org/10.1109/TMAG.2018.2852749.

[18] Y.Z. Zou, H. Wang, R.S. Yang, X.Y. Lai, J.W. Wan, G. Lin, D. Liu, Controlled synthesis and enhanced toluene-sensing properties of mesoporous $Ni_xCo_{1-x}Fe_2O_4$ nanostructured microspheres with tunable composite, Sens. Actuators, B 280 (2019) 227–234, https://doi.org/10.1016/j.snb.2018.10.030.

[19] H.R. Ebrahimi, M. Parish, G.R. Amiri, B. Bahraminejad, S. Fatahian, Synthesis, characterization and gas sensitivity investigation of $Ni_{0.5}Zn_{0.5}Fe_2O_4$ nanoparticles, J. Magn. Magn Mater. 414 (2016) 55–58, https://doi.org/10.1016/j.jmmm.2016.04.043.

[20] C. Mukherjee, R. Mondal, S. Dey, S. Kumar, J. Das, Nanocrystalline coppernickelzinc ferrite: efficient sensing materials for ethanol and acetone at room temperature, Ieee Sens. J. 17 (2017) 2662–2669, https://doi.org/10.1109/JSEN.2017.2684838.

[21] K.D. Wu, J.Z. Li, C. Zhang, Zinc ferrite based gas sensors: a review, Ceram. Int. 45 (2019) 11143–11157, https://doi.org/10.1016/j.ceramint.2019.03.086.

[22] X.L. Yang, S.F. Zhang, Q. Yu, P. Sun, F.M. Liu, H.Y. Lu, X. Yan, X. Zhou, X.S. Liang, Y. Gao, G.Y. Lu, Solvothermal synthesis of porous $CuFe_2O_4$ nanospheres for high performance acetone sensor, Sens. Actuators, B 270 (2018) 538–544, https://doi.org/10.1016/j.snb.2018.05.078.

[23] J.J. You, X. Chen, B.B. Zheng, X. Geng, C. Zhang, Suspension plasma-sprayed $ZnFe_2O_4$ nanostructured coatings for ppm-level acetone detection, J. Therm. Spray Technol. 26 (2017) 728–734, https://doi.org/10.1007/s11666-017-0536-7.

[24] R. Molavi, M.H. Sheikhi, Facile wet chemical synthesis of Al doped CuO nanoleaves for carbon monoxide gas sensor applications, Mater. Sci. Semicond. Process. 106 (2020) 104767, , https://doi.org/10.1016/j.mssp.2019.104767.

[25] C. Murugesan, N. Kambhala, S. Angappane, G. Chandrasekaran, Influence of Zn concentration on the structural and magnetic properties of nanocrystalline $Cu_{1-x}Zn_xFe_2O_4$ mixed ferrites synthesized using novel combustion method, J. Magn. Magn Mater. 443 (2017) 334–342, https://doi.org/10.1016/j.jmmm.2017.07.061.

[26] M. Ajmal, A. Maqsood, Influence of zinc substitution on structural and electrical properties of $Ni_{1-x}Zn_xFe_2O_4$ ferrites, Mat. Sci. Eng. B-Solid 139 (2007) 164–170, https://doi.org/10.1016/j.mseb.2007.02.004.

[27] R.D. Waldron, Infrared spectra of ferrites, Phys. Rev. 99 (1955) 1727–1735, https://doi.org/10.1103/PhysRev.99.1727.

[28] C.S. Lakshmi, C.S.L.N. Sridhar, G. Govindraj, S. Bangarraju, D.M. Potukuchi, Structural, magnetic and dielectric investigations in antimony doped nano-phased nickel-zinc ferrites, Physica B 459 (2015) 97–104, https://doi.org/10.1016/j.physb.2014.11.091.

[29] V.N. Nikolic, M.M. Vasic, D. Kisic, Observation of c-$CuFe_2O_4$ nanoparticles of the same crystallite size in different nanocomposite materials: the influence of Fe^{3+} cations, J. Solid State Chem. 275 (2019) 187–196, https://doi.org/10.1016/j.jssc.2019.04.007.

[30] W. Zhang, B. Quan, C. Lee, S.K. Park, X. Li, E. Choi, G.W. Diao, Y. Piao, One-step facile solvothermal synthesis of copper ferrite-graphene composite as a high-performance supercapacitor material, Acs Appl. Mater. Inter. 7 (2015) 2404–2414, https://doi.org/10.1021/am507014w.

[31] B.K. Chatterjee, A. Dey, C.K. Ghosh, K.K. Chattopadhyay, Interplay of bulk and surface on the magnetic properties of low temperature synthesized nanocrystalline cubic $Cu_{1-x}Zn_xFe_2O_4$ ($x = 0.00$, 0.02, 0.04 and 0.08), J. Magn. Magn Mater. 367 (2014) 19–32, https://doi.org/10.1016/j.jmmm.2014.04.059.

[32] S.L. Peng, Z.H. Wang, R. Liu, J. Bi, J.T. Wu, Controlled oxygen vacancies of $ZnFe_2O_4$ with superior gas sensing properties prepared via a facile one-step self-catalyzed treatment, Sens. Actuators, B 288 (2019) 649–655, https://doi.org/10.1016/j.snb.2019.03.056.

[33] X. Li, D. Lu, C. Shao, G. Lu, X. Li, Y. Liu, Hollow $CuFe_2O_4$/α-Fe_2O_3 composite with ultrathin porous shell for acetone detection at ppb levels, Sens. Actuators, B 258 (2018) 436–446, https://doi.org/10.1016/j.snb.2017.11.131.

[34] S. Bera, A.A.M. Prince, S. Velmurugan, P.S. Raghavan, R. Gopalan,

G. Panneerselvam, S.V. Narasimhan, J. Mater. Sci. 36 (2001) 5379–5384, https://doi.org/10.1023/A:1012488422484.

[35] G.J.P. Abreu, R. Paniago, H.D. Pfannes, Growth of ultra-thin FeO (100) films on Ag (100): a combined XPS, LEED and CEMS study, J. Magn. Magn Mater. 349 (2014) 235–239, https://doi.org/10.1016/j.jmmm.2013.08.059.

[36] N. Zhang, S.P. Ruan, J. Han, Y.Y. Yin, X. Li, C.X. Liu, S. Adimi, S.P. Wen, Y. Xu, Oxygen vacancies dominated CuO@$ZnFe_2O_4$ yolk-shell microspheres for robust and selective detection of xylene, Sens. Actuators, B 295 (2019) 117–126, https://doi.org/10.1016/j.snb.2019.05.073.

[37] R.W.J. Scott, S.M. Yang, G. Chabanis, N. Coombs, D.E. Williams, G.A. Ozin, Tin dioxide opals and inverted opals: near-ideal microstructures for gas sensors, Adv. Mater. 13 (2001) 1468–1472, https://doi.org/10.1002/1521-4095(200110)13:19<1468::AID-ADMA1468>3.0.CO;2-O.

[38] J.W. Ma, H.Q. Fan, W.M. Zhang, J.N. Sui, C. Wang, M.C. Zhang, N. Zhao, A.K. Yadav, W.J. Wang, W.Q. Dong, S.R. Wang, High sensitivity and ultra-low detection limit of chlorine gas sensor based on In_2O_3 nanosheets by a simple template method, Sens. Actuators, B 305 (2020) 127456, , https://doi.org/10.1016/j.snb.2019.127456.

[39] L. Sun, J. Sun, N. Han, D. Liao, S. Bai, X. Yang, R. Luo, D. Li, A. Chen, rGO decorated W doped $BiVO_4$ novel material for sensing detection of trimethylamine, Sens. Actuators, B 298 (2019) 126749, , https://doi.org/10.1016/j.snb.2019.126749.

[40] L. Lv, Y. Wang, P. Cheng, B. Zhang, F. Dang, L. Xu, Ultrasonic spray pyrolysis synthesis of three-dimensional $ZnFe_2O_4$-based macroporous spheres for excellent sensitive acetone gas sensor, Sens. Actuators, B 297 (2019) 126755, , https://doi.org/10.1016/j.snb.2019.126755.

[41] X.F. Wang, W. Ma, F. Jiang, E.-S. Cao, K.-M. Sun, L. Cheng, X.-Z. Song, Prussian Blue analogue derived porous $NiFe_2O_4$ nanocubes for low-concentration acetone sensing at low working temperature, Chem. Eng. J. 338 (2018) 504–512, https://doi.org/10.1016/j.cej.2018.01.072.

[42] H.J. Zhang, L.Z. Liu, X.R. Zhang, S. Zhang, F.N. Meng, Microwave-assisted solvothermal synthesis of shape-controlled $CoFe_2O_4$ nanoparticles for acetone sensor, J. Alloys Compd. 788 (2019) 1103–1112, https://doi.org/10.1016/j.jallcom.2019.03.009.

[43] C.H. Zhao, W.Z. Lan, H.M. Gong, J.L. Bai, R. Rarnachandran, S. Liu, F. Wang, Highly sensitive acetone-sensing properties of Pt-decorated $CuFe_2O_4$ nanotubes prepared by electrospinning, Ceram. Int. 44 (2018) 2856–2863, https://doi.org/10.1016/j.ceramint.2017.11.032.

[44] M.S. Khandekar, N.L. Tarwal, I.S. Mulla, S.S. Suryavanshi, Nanocrystalline Ce doped $CoFe_2O_4$ as an acetone gas sensor, Ceram. Int. 40 (2014) 447–452, https://doi.org/10.1016/j.ceramint.2013.06.021 2014.

[45] Z.J. Song, H.M. Chen, S.S. Bao, Z.X. Xie, Q. Kuang, L.S. Zheng, Nanosheet-assembled, hollowed-out hierarchical gamma-Fe_2O_3 microrods for high-performance gas sensing, J. Mater. Chem. 8 (2020) 3754–3762, https://doi.org/10.1039/c9ta12052a.

[46] N.S. Shuman, W.R. Stevens, T. Baer, Dissociation dynamics of energy-selected acetic acid ions: the gas phase heat of formation of the acetyl ion, Int. J. Mass Spectrom. 294 (2010) 88–92, https://doi.org/10.1016/j.ijms.2010.05.021.

[47] X.J. Liu, K.R. Zhao, X.L. Sun, X.P. Duan, C. Zhang, X.J. Xu, Electrochemical sensor to environmental pollutant of acetone based on Pd-loaded on mesoporous In_2O_3 architecture, Sens. Actuators, B 290 (2019) 217–225, https://doi.org/10.1016/j.snb.2019.03.139.

[48] W. Zhang, Y.B. Shen, J. Zhang, H.S. Bi, S.K. Zhao, P.F. Zhou, C. Han, D.Z. Wei, N. Cheng, Low-temperature H_2S sensing performance of Cu-doped $ZnFe_2O_4$ nanoparticles with spinel structure, Appl. Surf. Sci. 470 (2019) 581–590, https://doi.org/10.1016/j.apsusc.2018.11.164.

[49] A. Sutka, G. Mezinskis, A. Lusis, D. Jakovlevs, Influence of iron non-stoichiometry on spinel zinc ferrite gas sensing properties, Sens. Actuators, B 171 (2012) 204–209, https://doi.org/10.1016/j.snb.2012.03.012.

[50] X.P. Li, Z.Y. Gu, J.H. Cho, H.W. Sun, P. Kurup, Tin-copper mixed metal oxide nanowires: synthesis and sensor response to chemical vapors, Sens. Actuators, B 158 (2011) 199–207, https://doi.org/10.1016/j.snb.2011.06.004.

[51] S. Saini, J. Shah, R.K. Kotnala, K.L. Yadav, Nickel substituted oxygen deficient nanoporous lithium ferrite based green energy device hydroelectric cell, J. Alloys Compd. 827 (2020) 154334, , https://doi.org/10.1016/j.jallcom.2020.154334.

[52] M.R. Alenezi, A.S. Alshammari, K.D. Jayawardena, M.J. Beliatis, S.J. Henley, S.R. Silva, Role of the exposed polar facets in the performance of thermally and UV activated ZnO nanostructured gas sensors, J. Phys. Chem. C Nanomater Interfaces 117 (2013) 17850–17858, https://doi.org/10.1021/jp4061895.